Stable Spectral Difference Approach Using Raviart-Thomas Elements for 3D Computations on Tetrahedral Grids

Adèle Veilleux, Guillaume Puigt, Hugues Deniau, Guillaume Daviller

Stable Spectral Difference approach using Raviart-Thomas elements for 3D computations on tetrahedral grids

Adèle Veilleux[a,b,*], Guillaume Puigt[a], Hugues Deniau[a], Guillaume Daviller[b]

[a] *ONERA/DMPE, Université de Toulouse, F-31055 Toulouse, France*
[b] *Centre Européen de Recherche et de Formation Avancée en Calcul Scientifique (CERFACS), 42 avenue Gaspard Coriolis, 31057 Toulouse Cedex 01, France*

Abstract

In this paper, the Spectral Difference approach using Raviart-Thomas elements (SDRT) is formulated for the first time on tetrahedral grids. To determine stable formulations, a Fourier analysis is conducted for different SDRT implementations, i.e. different interior flux points locations. This stability analysis demonstrates that using interior flux points located at the Shunn-Ham quadrature rule points leads to linearly stable SDRT schemes up to the third order. For higher orders of accuracy, a significant impact of the position of flux points located on faces is shown. The Fourier analysis is then extended to the coupled time-space discretization and stability limits are determined. Additionally, a comparison between the number of interior FP required for the SDRT scheme and the Flux Reconstruction method is proposed and shows that the two approaches always differ on the tetrahedron. Unsteady validation test cases include a convergence study using the Euler equations and the simulation of the Taylor-Green vortex.

Keywords: High-order, Spectral Difference, Raviart-Thomas, Tetrahedra.

Acknowledgments

Dr. Guillaume Puigt is partially supported by LMA2S (Laboratoire de Mathématiques Appliquées à l'Aéronautique et au Spatial), the Applied Mathematics Lab of ONERA.

1. Introduction

Numerical schemes using piecewise continuous polynomials approximation are an efficient way to obtain high-order accuracy on unstructured grids. Their interest comes from the possibility to handle a high-order representation of the unknowns using polynomials and a compact stencil, which allows to achieve a good parallel efficiency. By nature, the solution is sought under the form of a polynomial defined locally, in each mesh cell. Since continuity is not required at cell interfaces, a Riemann solver is introduced to define the flux from two different extrapolated quantities. In the case of the most popular high-order discontinuous method called the Discontinuous Galerkin (DG) approach, the full system of equations is built using the weak formulation, as in the standard finite element method. For a solution approximated as a polynomial of degree p defined on a given basis, test functions are also polynomials of degree p and quadrature rules are necessary to compute either volume or surface integrals at the appropriate order of accuracy. Depending on the definition of the solution approximation, different DG implementations are possible. On one hand, the DG method is said nodal if the solution approximation is defined by an interpolation from solution values

*Corresponding author
Email addresses: Adele.Veilleux@onera.fr (Adèle Veilleux), Guillaume.Puigt@onera.fr (Guillaume Puigt), Hugues.Deniau@onera.fr (Hugues Deniau), Guillaume.Daviller@cerfacs.fr (Guillaume Daviller)

at dedicated points (such as Lagrange interpolation). On the other hand, if the solution approximation is expressed as a linear combination over a basis, the DG method is modal, since coefficients from the linear combination are simply modes of the solution.

An advantage of standard DG methods (either nodal or modal) is their ability to deal with unstructured mesh. The formulation naturally accounts for simplex cells (tetrahedron in 3D), which are the standard elements for (automatic) mesh generation on complex geometry. The literature on the Discontinuous Galerkin method on simplex cells is very rich ([1, 2, 3, 4, 5, 6] for example). However, using the integral formulation leads to a heavy computational cost to obtain a high-order of accuracy since high-order surface and volume integral evaluations using quadrature rules are required.

The main objective of the present paper is to draw attention to more recent classes of numerical methods using piecewise polynomials based on the strong form of equations for tetrahedral grids. Alternative methods explicitly compute two polynomials, one for the solution and one for the flux. For consistency, the flux divergence must lie in the same polynomial space as the solution. Today, there are essentially two different methods based on the strong form.

The first method is called the Correction Procedure for Reconstruction (CPR) or the Flux Reconstruction (FR) approach. Following the pioneering work of Huynh [7], the solution and the flux approximations are first defined with the same polynomial degree from a set of points called solution points. This leads to a flux polynomial inconsistent with the solution since its divergence loses one degree. In addition, the flux is defined from the solution and therefore not continuous at cell interfaces. To remedy both problems, a correction polynomial is introduced. This correction polynomial is defined from the flux at the cell interfaces at a degree equal to the one of the solution plus one. Several FR reconstructions can be built depending on the definition of the correction polynomial, associated with different properties and capabilities. Several studies investigate the FR implementation on tetrahedral cells. The class of Vincent-Castonguay-Jameson-Huynh (VCJH) [8] schemes were first extended to tetrahedral elements by Williams and Jameson [9]. The effect of the solution point location was studied in [10, 11] to determine their effect on the stability and the accuracy of FR schemes on tetrahedral grids. Both works indicate that the best choice in terms of stability and accuracy is to locate the solution points following the Shunn-Ham quadrature rule [12]. The FR method was then used to simulate turbulent flows on tetrahedral meshes by Bull and Jameson [13].

The second approach is called the Spectral Difference method. Initiated by Kopriva [14] as the staggered-grid Chebyshev multi-domain method for structured grids, it was then introduced for triangular elements together with the naming Spectral Difference (SD) [15]. The standard formulation was found unstable on triangles for an order of accuracy strictly greater than two by Van Abeele [16]. Researchers essentially focused attention on unstructured quadrilateral and hexahedral grids, following a tensorial formulation from the 1D stable discretization. An alternative formulation called the Spectral Difference method using the Raviart-Thomas space (SDRT) was introduced for Euler equations in [17] on triangles and proven to be linearly stable up to the fourth-order under a Fourier stability analysis originally initiated by May and Schöberl [18]. The SDRT method was then formulated to simulate 2D viscous flows on unstructured hybrid grids up to the fourth-order by Li *et al.* [19] and used for the simulation of vortex-induced vibrations using a sliding-mesh method on hybrid grids by Qiu *et al.* [20]. Finally, the method was extended to higher orders of accuracy in [21] for triangular and 2D hybrid grids. To the author's knowledge, the literature on the Spectral Difference is dedicated to quadrilateral, triangular and hexahedral cells.

In this context, the present paper introduces the first linearly stable formulation of the Spectral Difference method on 3D simplex cells. The paper is organized as follows. In Sec. 2, the SDRT scheme is presented on tetrahedral cells. The linear stability of the SDRT method based on interior FP located at known quadrature rules points is studied using Fourier analysis in Sec. 3. Stable formulations are determined up to the third-order of accuracy. The influence of flux points located on faces for $p = 3$ is highlighted. The Fourier analysis is then extended to the coupled time-space discretization. Unsteady validation test cases are presented in Sec. 4 and include a convergence study using the Euler equations and the simulation of the Taylor-Green vortex.

2. Spectral Difference Scheme on Tetrahedral Grids

2.1. Reference Domain

Let us consider the following 3D scalar conservation law under its differential form:

$$\frac{\partial u(\mathbf{x},t)}{\partial t} + \nabla \cdot \mathbf{f}(u) = 0, \quad \text{in } \Omega \times [0, t_f], \tag{1}$$

where u is the state variable, $\mathbf{f} = (f, g, h)$ is the flux vector where f, g and h are flux densities in the x, y and z directions respectively and ∇ is the differential operator in the physical domain $\mathbf{x} = (x, y, z)$. The computational domain Ω is discretized into N non-overlapping tetrahedral cells and the i-th element is denoted Ω_i:

$$\Omega = \bigcup_{i=1}^{N} \Omega_i. \tag{2}$$

For implementation simplicity, Eq. (1) is solved in the reference domain. Each cell Ω_i of the domain Ω is transformed into a reference tetrahedron $\mathcal{T}_e := \{(\xi, \eta, \zeta) : 0 \le \xi, \eta, \zeta \le 1, \xi + \eta + \zeta \le 1\}$. The transformation can be written as:

$$\begin{pmatrix} x \\ y \\ z \end{pmatrix} = \sum_{i=1}^{N_p} M_i(\xi, \eta, \zeta) \begin{pmatrix} x_i \\ y_i \\ z_i \end{pmatrix}, \tag{3}$$

where (x_i, y_i, z_i) are the Cartesian coordinates of the N_p vertices of the cells and $M_i(\xi, \eta, \zeta)$ are the shape functions. The Jacobian matrix of the transformation given by Eq. (3) from the physical (x, y, z) to the reference domain (ξ, η, ζ) takes the following form:

$$J = \frac{\partial(x, y, z)}{\partial(\xi, \eta, \zeta)} = \begin{bmatrix} x_\xi & x_\eta & x_\zeta \\ y_\xi & y_\eta & y_\zeta \\ z_\xi & z_\eta & z_\zeta \end{bmatrix}. \tag{4}$$

For a non-singular transformation, the inverse transformation is related to the Jacobian matrix according to:

$$\frac{\partial(\xi, \eta, \zeta)}{\partial(x, y, z)} = \begin{bmatrix} \xi_x & \xi_y & \xi_z \\ \eta_x & \eta_y & \eta_z \\ \zeta_x & \zeta_y & \zeta_z \end{bmatrix} = J^{-1}. \tag{5}$$

In the reference domain, Eq. (1) becomes:

$$\frac{\partial \hat{u}(\boldsymbol{\xi}, t)}{\partial t} + \hat{\nabla} \cdot \hat{\mathbf{f}} = 0, \tag{6}$$

where $\hat{\nabla}$ is the differential operator in the reference domain, $\boldsymbol{\xi} = (\xi, \eta, \zeta)$ are the coordinates in the reference domain and $\hat{u}$, $\hat{\mathbf{f}}$ are the solution and the flux in the reference domain defined by:

$$\hat{u} = |J| u, \tag{7}$$

and

$$\hat{\mathbf{f}} = |J| J^{-1} \mathbf{f}. \tag{8}$$

2.2. SDRT scheme on tetrahedra

The SDRT scheme introduced in [22, 17] for triangles is here extended to 3D simplex cells, i.e. tetrahedra.

2.2.1. Solution polynomial

The solution $\hat{u}$ is approximated on the reference tetrahedron $\mathcal{T}_e$ by a polynomial of degree p, $\hat{u}_h(\boldsymbol{\xi}) \in \mathbb{P}_p$, through a set of distinct Solution Points (SP) $\boldsymbol{\xi}_j, j \in [\![1, N_{SP}]\!]$ where

$$N_{SP} = \frac{(p+1)(p+2)(p+3)}{6}, \tag{9}$$

and

$$\mathbb{P}_p = \text{span}\{\xi^i \eta^j \zeta^k, 0 \le i, 0 \le j, 0 \le k \text{ and } i+j+k \le p\}. \tag{10}$$

The polynomial $\hat{u}_h(\boldsymbol{\xi})$ is expanded using a modal representation:

$$\hat{u}_h(\boldsymbol{\xi}) = \sum_{m=1}^{N_{SP}} \bar{u}_m \, \Phi_m(\boldsymbol{\xi}), \tag{11}$$

where $\Phi_m(\boldsymbol{\xi}) \in \mathbb{P}_p$ is a complete polynomial basis and $\bar{u}_m$ are the modal basis coefficients. Coefficients $\bar{u}_m$ are determined by performing a collocation projection at the points $\boldsymbol{\xi}_j$:

$$\hat{u}_h(\boldsymbol{\xi}_j) = \hat{u}_j = \sum_{m=1}^{N_{SP}} \bar{u}_m \, \Phi_m(\boldsymbol{\xi}_j), \tag{12}$$

$$\bar{u}_m = \sum_{m=1}^{N_{SP}} \hat{u}_j \left(\Phi_m(\boldsymbol{\xi}_j)\right)^{-1}. \tag{13}$$

The basis Φ is chosen as the orthonormal Proriol-Koornwinder-Dubiner (PKD) [23, 24, 25] basis, given on the tetrahedron for a polynomial approximation of degree p as:

$$\Phi_{i,j,k} = \sqrt{(i+1/2)(i+j+1)(i+j+k+3/2)}\, P_i^{0,0}(\xi) \left(\frac{1-\eta}{2}\right)^i P_j^{2i+1,0}(\eta) \left(\frac{1-\zeta}{2}\right)^{i+j} P_k^{2(i+j+1),0}(\zeta), \quad i+j+k \le p, \tag{14}$$

where $P_n^{\alpha,\beta}$ are the corresponding n-th order Jacobi polynomials on the interval $[-1, 1]$ which, under the Jacobi weight $(1-x)^\alpha (1+x)^\beta$ are orthogonal polynomials. For simplicity, the subscript (i, j, k) can be replaced by the single index m, $m \in [\![1, N_{SP}]\!]$ with any arbitrary bijection $m \equiv m(i, j, k)$. The polynomial approximation $\hat{u}_h$ of the solution $\hat{u}$ is thus defined in the reference space by:

$$\hat{u}_h(\boldsymbol{\xi}) = \sum_{m=1}^{N_{SP}} \hat{u}_j \left(\Phi_m(\boldsymbol{\xi}_j)\right)^{-1} \Phi_m(\boldsymbol{\xi}). \tag{15}$$

2.2.2. Solution computation at flux points

To compute the flux values at flux points (FP), we first have to determine the solution values at those points. With the polynomial distribution given by Eq. (15), the solution at the FP (denoted $\boldsymbol{\xi}_k$) can be computed as:

$$\hat{u}_h(\boldsymbol{\xi}_k) = \sum_{m=1}^{N_{SP}} \hat{u}_j \left(\Phi_m(\boldsymbol{\xi}_j)\right)^{-1} \Phi_m(\boldsymbol{\xi}_k) = \sum_{m=1}^{N_{SP}} \hat{u}_j \left(\mathcal{V}_{j,m}\right)^{-1} \Phi_m(\boldsymbol{\xi}_k), \tag{16}$$

where $\mathcal{V}$ is the generalized Vandermonde matrix. Numerically, the extrapolation step is represented by the transfer matrix $\mathbf{T}_{kj} = \left[\left(\mathcal{V}_{j,m}\right)^{-1} \Phi_m(\boldsymbol{\xi}_k)\right]$.

2.2.3. Definition of the flux polynomial from the set of fluxes at flux points

The flux function in the reference domain is approximated by $\hat{\mathbf{f}}_h$ in the Raviart-Thomas (RT) space (see Appendix A for details) as:

$$\hat{\mathbf{f}}_h(\boldsymbol{\xi}) = \sum_{k=1}^{N_{FP}} \hat{f}_k \boldsymbol{\psi}_k(\boldsymbol{\xi}), \tag{17}$$

where N_{FP} is the number of degrees of freedom needed to represent a vector-valued function in the RT_p space:

$$N_{FP} = \frac{1}{2}(p+1)(p+2)(p+4), \tag{18}$$

and $\boldsymbol{\psi}_k$ are interpolation functions which form a basis in the RT space with the property:

$$\boldsymbol{\psi}_j(\boldsymbol{\xi}_k) \cdot \hat{\mathbf{n}}_k = \delta_{jk}, \tag{19}$$

where δ is the Kronecker symbol and $\hat{\mathbf{n}}_k$ are the unit normal vectors defined at FP. As for the SDRT formulation on triangles, for interior FP, one physical point is associated with d degrees of freedom, where d is the dimension, through the definition of unit vectors in different directions. In 3D, the unit vectors for interior FPs are $\hat{\mathbf{n}} = (1,0,0)^\intercal$, $\hat{\mathbf{n}} = (0,1,0)^\intercal$ and $\hat{\mathbf{n}} = (0,0,1)^\intercal$ in the reference element.

Scalar flux values $\hat{f}_k$ at FP on which the polynomial approximation given by Eq. (17) relies on are determined in the same manner as for 2D simplex cells. For a first-order partial differential equation, they are given as:

$$\hat{f}_k = \begin{cases} \hat{\mathbf{f}}_k \cdot \hat{\mathbf{n}}_k = |J| J^{-1} \mathbf{f}_k(u_h(\boldsymbol{\xi}_k)) \cdot \hat{\mathbf{n}}_k, & \boldsymbol{\xi}_k \in \mathcal{T}_e \setminus \partial\mathcal{T}_e, \\ \left(\hat{\mathbf{f}}_k \cdot \hat{\mathbf{n}}_k\right)^* = \left(\mathbf{f}_k \cdot |J| (J^{-1})^\intercal \hat{\mathbf{n}}_k\right)^*, & \boldsymbol{\xi}_k \in \partial\mathcal{T}_e. \end{cases} \tag{20}$$

where $\left(\hat{\mathbf{f}}_k \cdot \hat{\mathbf{n}}_k\right)^*$ is the standard numerical flux in the reference element and $u_h(\boldsymbol{\xi}_k) = \frac{1}{|J|}\hat{u}_h(\boldsymbol{\xi}_k)$ is the approximated solution in the physical domain.

2.2.4. Differentiation of the flux polynomial in the set of solution points

Once the flux vector is approximated on the reference element by Eq. (17), it can be differentiated at SP:

$$\begin{aligned} \hat{\nabla} \cdot \hat{\mathbf{f}}(u) &= \left(\hat{\nabla} \cdot \hat{\mathbf{f}}_h\right)(\boldsymbol{\xi}_j) \\ &= \sum_{k=1}^{N_{FP}} \hat{f}_k \left(\hat{\nabla} \cdot \boldsymbol{\psi}_k\right)(\boldsymbol{\xi}_j). \end{aligned} \tag{21}$$

Numerically, the differentiation step is represented by the differentiation matrix $\mathbf{D}_{jk} = \left[\left(\hat{\nabla} \cdot \boldsymbol{\psi}_k\right)(\boldsymbol{\xi}_j)\right]$. The term $\left(\hat{\nabla} \cdot \boldsymbol{\psi}_k\right)(\boldsymbol{\xi}_j)$ in Eq. (21) is fully defined through the determination of the vector-valued interpolation basis functions $\boldsymbol{\psi}_k$ and their derivatives detailed in [21].

The final form of the SDRT scheme can be written for each degree of freedom of the solution function in each cell i as:

$$\frac{d\hat{u}_j^{(i)}}{dt} + \sum_{k=1}^{N_{FP}} \hat{f}_k^{(i)} \left(\hat{\nabla} \cdot \boldsymbol{\psi}_k\right)(\boldsymbol{\xi}_j) = 0, \quad j \in [\![1, N_{SP}]\!], \quad i \in [\![1, N]\!]. \tag{22}$$

and the solution can be time-integrated using any standard time integration scheme (Runge-Kutta scheme for instance).

3. Linear Stability Analysis of the SDRT Formulation

The SDRT formulation on tetrahedral elements was introduced but the position of the flux points is still an open question. In this section, the position of the flux points is described and the stability of the formulation is justified by a Fourier analysis.

3.1. Choice of Solution Points and Flux Points Location

The location of SP and FP needs to be chosen for the reference tetrahedron. The number of SP and FP are respectively given by:

$$N_{SP} = \frac{1}{6}(p+1)(p+2)(p+3), \tag{23}$$

$$N_{FP} = \frac{1}{2}(p+1)(p+2)(p+4). \tag{24}$$

Remark: In this article, the FP location is constrained so that there are no points located at vertices and on edges of the tetrahedron. Actually, if such points were used, FP could be shared by more than two cells and a multi-dimensional Riemann solver should be used. If the interface FP are located on the face (and not on edges), such a configuration will never appear.

Applying this requirement, the number of FP located on each face is equal to $(p+1)(p+2)/2$, which corresponds to the number of SP on a triangle. By choosing their location to be the same as the SP on a triangle, we ensure that a tetrahedral and a prismatic element will share the same FP on faces, avoiding the need to apply mortar techniques. For $p \in [\![1,2]\!]$, the face FP are thus located following the Williams-Shunn-Jameson quadrature rule [26]. The number of interior FP is then given by:

$$N_i = \frac{1}{2}p(p+1)(p+2). \tag{25}$$

Since each physical FP is counted as three separated DoF, the number of interior physical FP for which the position has to be settled is $N_{pi} = \frac{1}{6}p(p+1)(p+2)$. The number of SP and physical interior FP is summarized in Table 1. It can be noted that the number of physical interior FP for a SDRT_p scheme corresponds to the number of SP for a SDRT_{p-1} scheme.

p	N_{SP}	N_{pi}
1	4	1
2	10	4
3	20	10
4	35	20
5	56	35
6	84	56

Table 1: Number of SP and physical interior FP for SDRT scheme on tetrahedral elements

To set the SP and physical interior FP locations on tetrahedral elements, quadrature rules available in the literature are studied. To be suitable for the SDRT implementation, the quadrature rules should not have points located on corner, edge or face. Among the possible quadratures, three quadrature rules are found to lead to the appropriate number of points for each degree p while fulfilling this requirement: the Newton-Cotes Open (NCO) [27], the Vioreanu-Rokhlin [28] and the Shunn-Ham [12] quadrature rules. Since those quadrature rules are suitable for each degree p, they can be used for both the SP and the physical interior FP by choosing the adequate quadrature order. Other quadrature rules can lead to the proper number of points for a given degree p and will be given below. The SP are chosen to be located at the Shunn-Ham quadrature points. For the physical interior FP:

- For $p = 1$, all the studied quadrature rules led to the same physical interior point located at $(x, y, z) = (0.25, 0.25, 0.25)$ in the reference domain.
- For $p = 2$, it is noted that several quadrature rules lead to the very same set of points (Keast [29], Vioreanu-Rokhlin [28], Shunn-Ham [12], Witherden-Vincent [30], Yu [31], Hammer-Marlowe-Stroud [32], Liu-Vinokur [33]). This set of point will be referred here as the Shunn-Ham quadrature rule. Three other quadrature rules containing four points will be studied: the Jakowiec-Sukumar [34], the Xiao-Gimbutas [35] and the NCO [27].

- For $p > 2$, the studied quadrature rules are Shunn-Ham, Vioreanu-Rokhlin and NCO, which contain the appropriate number of points for each p.

3.2. Matrix Form

We consider the 3D linear advection equation:

$$\frac{\partial u(\mathbf{x},t)}{\partial t} + \nabla \cdot \mathbf{f} = 0, \ \text{ in } \Omega \times [0, t_f] \tag{26}$$

within a domain $\Omega = [0, L]^3$ with periodic boundary conditions, where u is a conserved scalar quantity and $\mathbf{f} = \mathbf{c} \cdot u$ is the flux. The velocity vector is $\mathbf{c} = (\sin\theta_2 \cos\theta_1, \sin\theta_2 \sin\theta_1, \cos\theta_2)^\top$ where $(\theta_1, \theta_2) \in [0, \pi/4]$. The domain Ω is meshed as a Cartesian mesh composed of $N_x \times N_y \times N_z$ hexahedral elements of size $\Delta x \times \Delta y \times \Delta z$, with $\Delta x = \Delta y = \Delta z$. Each hexahedral cell is then divided into tetrahedron. A hexahedron can be decomposed into a minimum of five tetrahedral elements, but to ensure the periodicity, six tetrahedrons are required. The six tetrahedrons of the hexahedral cell (i_1, i_2, i_3) are denoted $T^{i_1,i_2,i_3,1}, T^{i_1,i_2,i_3,2}, T^{i_1,i_2,i_3,3}, T^{i_1,i_2,i_3,4}, T^{i_1,i_2,i_3,5}, T^{i_1,i_2,i_3,6}$ and are represented in Fig. 1.

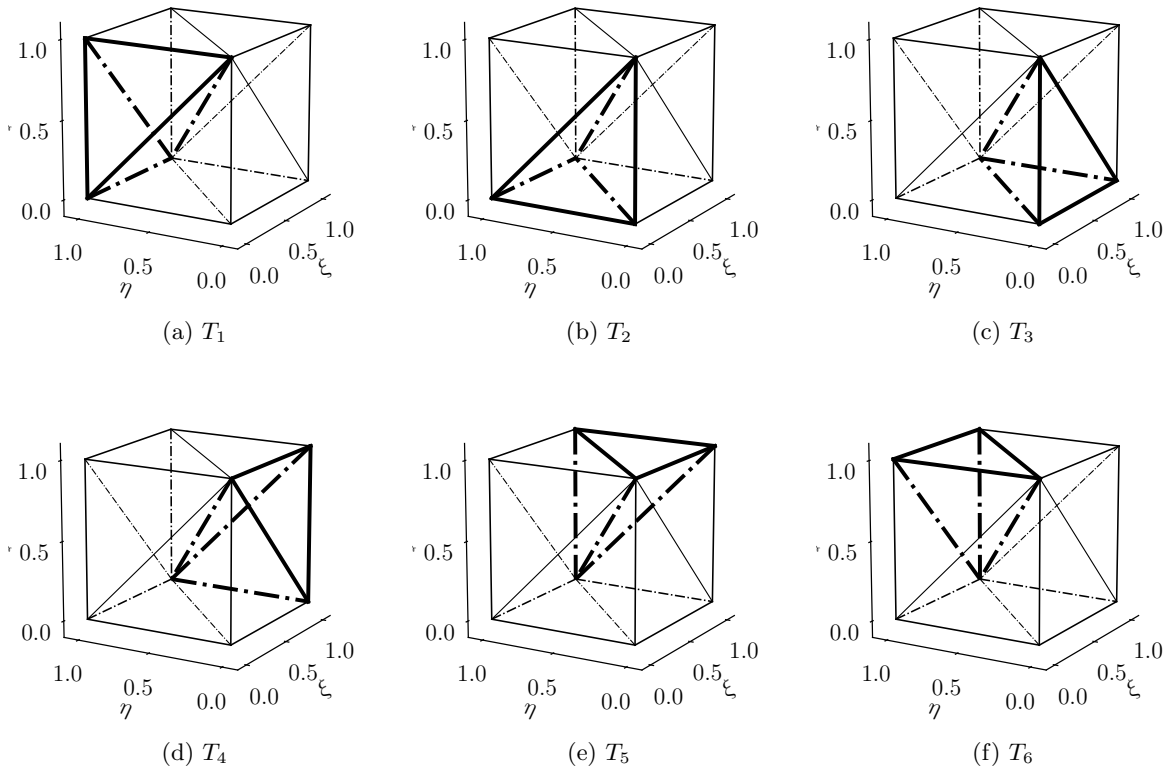

(a) T_1 (b) T_2 (c) T_3

(d) T_4 (e) T_5 (f) T_6

Figure 1: Computational domain for the Fourier stability analysis on tetrahedral elements

Defining:

$$\hat{\mathbf{U}}_j^{i_1,i_2,i_3} = [\hat{\mathbf{U}}_j^{i_1,i_2,i_3,1}, \hat{\mathbf{U}}_j^{i_1,i_2,i_3,2}, \hat{\mathbf{U}}_j^{i_1,i_2,i_3,3}, \hat{\mathbf{U}}_j^{i_1,i_2,i_3,4}, \hat{\mathbf{U}}_j^{i_1,i_2,i_3,5}, \hat{\mathbf{U}}_j^{i_1,i_2,i_3,6}]^\top, \tag{27}$$

as the vector collecting the solution in the reference domain on the six tetrahedrons for each SP $j \in [\![1, N_{SP}]\!]$ on cell (i_1, i_2, i_3), the SDRT spatial discretization using an upwind flux on this mesh takes the form:

$$\begin{aligned}\frac{d\hat{\mathbf{U}}_j^{i_1,i_2,i_3}}{dt} = -\frac{\|\mathbf{c}\|}{\Delta x}\Big[&\mathbf{M}^{0,0,0}\,\hat{\mathbf{U}}_j^{i_1,i_2,i_3} + \mathbf{M}^{-1,0,0}\,\hat{\mathbf{U}}_j^{i_1-1,i_2,i_3} \\ &+ \mathbf{M}^{+1,0,0}\,\hat{\mathbf{U}}_j^{i_1+1,i_2,i_3} \\ &+ \mathbf{M}^{0,-1,0}\,\hat{\mathbf{U}}_j^{i_1,i_2-1,i_3} \\ &+ \mathbf{M}^{0,+1,0}\,\hat{\mathbf{U}}_j^{i_1,i_2+1,i_3} \\ &+ \mathbf{M}^{0,0,-1}\,\hat{\mathbf{U}}_j^{i_1,i_2,i_3-1} \\ &+ \mathbf{M}^{0,0,+1}\,\hat{\mathbf{U}}_j^{i_1,i_2,i_3+1}\Big].\end{aligned} \tag{28}$$

In Eq. (28), $\mathbf{M}^{0,0,0}$, $\mathbf{M}^{-1,0,0}$, $\mathbf{M}^{+1,0,0}$, $\mathbf{M}^{0,-1,0}$, $\mathbf{M}^{0,+1,0}$, $\mathbf{M}^{0,0,-1}$ and $\mathbf{M}^{0,0,+1}$ are matrices of size $[6N_{SP}, 6N_{SP}]$ containing the three steps of the spatial discretization (extrapolation, flux computation and differentiation), which depend on the advection angles as well as on the SP and FP locations. The exact formulation of those matrices is given in Appendix B.

3.3. Fourier Stability Analysis

To perform the Fourier stability analysis on tetrahedral elements, the discretized numerical solution is assumed under the form of a planar harmonic wave:

$$\hat{\mathbf{U}}^{i_1,i_2,i_3} = \tilde{\mathbf{U}} \exp\Big(I\mathbf{k}\,(i_1\mathbf{x} + i_2\mathbf{y} + i_3\mathbf{z})\Big), \tag{29}$$

where

$$(\mathbf{x}, \mathbf{y}, \mathbf{z}) = \left(\begin{pmatrix}\Delta x\\0\\0\end{pmatrix}, \begin{pmatrix}0\\\Delta x\\0\end{pmatrix}, \begin{pmatrix}0\\0\\\Delta x\end{pmatrix}\right) \tag{30}$$

are the vectors defining the mesh, $\tilde{\mathbf{U}}$ is a complex vector of dimension $6N_{SP}$, independent of i_1, i_2 and i_3, and

$$\mathbf{k} = k\begin{pmatrix}\cos\vartheta_1 \sin\vartheta_2\\ \sin\vartheta_1 \sin\vartheta_2\\ \cos\vartheta_2\end{pmatrix}, \tag{31}$$

k being the wave number of the harmonic wave and $(\vartheta_1, \vartheta_2)$ its orientation angles. Using non-dimensional quantities, Eq. (29) becomes:

$$\hat{\mathbf{U}}^{i_1,i_2,i_3} = \tilde{\mathbf{U}} \exp\Big(I\kappa\,(i_1 \cos\vartheta_1 \sin\vartheta_2 + i_2 \sin\vartheta_1 \sin\vartheta_2 + i_3 \cos\vartheta_2)\Big), \tag{32}$$

$\kappa = k\Delta x$ being the grid frequency. Injecting Eq. (32) into Eq. (28), one gets:

$$\begin{aligned}\frac{d\tilde{\mathbf{U}}}{dt} = -\frac{\|\mathbf{c}\|}{\Delta x}\Big[&\mathbf{M}^{0,0,0} + \mathbf{M}^{-1,0,0}\exp(-I\kappa\cos\vartheta_1\sin\vartheta_2) \\ &+ \mathbf{M}^{+1,0,0}\exp(I\kappa\cos\vartheta_1\sin\vartheta_2) \\ &+ \mathbf{M}^{0,-1,0}\exp(-I\kappa\sin\vartheta_1\sin\vartheta_2) \\ &+ \mathbf{M}^{0,+1,0}\exp(I\kappa\sin\vartheta_1\sin\vartheta_2) \\ &+ \mathbf{M}^{0,0,-1}\exp(-I\kappa\cos\vartheta_2) \\ &+ \mathbf{M}^{0,0,+1}\exp(I\kappa\cos\vartheta_2)\Big]\,\tilde{\mathbf{U}} \\ = \frac{\|\mathbf{c}\|}{\Delta x}\,&\mathbf{M}_z\,\tilde{\mathbf{U}}.\end{aligned} \tag{33}$$

Using the eigenvalue analysis, the SDRT spatial discretization is stable under a Fourier stability analysis if the real part of all eigenvalues of the matrix $\mathbf{M}_z$ are non-positive, i.e. if $\mathrm{Re}(\lambda_{\mathbf{M}_z}) \leq 0$. The complete spectrum of the SDRT spatial operator $\lambda_{\mathbf{M}_z}$ is obtained by computing the eigenvalues of $\mathbf{M}_z$ over the grid frequency $\kappa \in [-\pi, \pi]$ considering $(\vartheta_1, \vartheta_2) \in [0, 2\pi]$. For $p = 1$, the spectrum of $\mathbf{M}_z$ is plotted in Fig. 2a for $(\theta_1, \theta_2) \in (0, \pi/8, \pi/4)^2$. A closer view on the spectrum allows to see the non-positivity of $\mathrm{Re}(\lambda_{\mathbf{M}_z})$ and to establish the stability of the spatial discretization.

For $p = 2$, there are 4 interior physical FP. In Fig. 2b, the spectrum of the SDRT_2 discretization using the Shunn-Ham rule for interior FP is plotted for $(\theta_1, \theta_2) \in (0, \pi/8, \pi/4)^2$. A closer view on the spectrum allows to see the non-positivity of $\mathrm{Re}(\lambda_{\mathbf{M}_z})$, indicating a stable SDRT scheme.

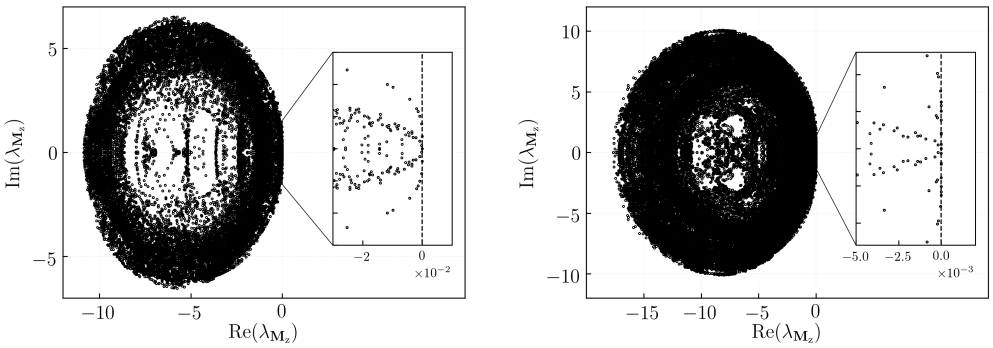

(a) SDRT_1 (b) SDRT_2, Shunn-Ham rule

Figure 2: Spectrum of matrix $\mathbf{M}_z$ for stable SDRT schemes on tetrahedral elements, $(\theta_1, \theta_2) \in (0, \pi/8, \pi/4)^2$

In Fig. 3, the spectrum is plotted for the particular case $(\theta_1, \theta_2) = (0, 0)$ for the three other quadrature rules: the Jakowiec-Sukumar (Fig. 3a), the Xiao-Gimbutas (Fig. 3b) and the NCO (Fig. 3c). The SDRT scheme using those three quadrature rules is found unstable with $\max(\mathrm{Re}(\lambda_{\mathbf{M}_z})) \sim 3 \cdot 10^{-4}$ for Jakowiec-Sukumar, $\max(\mathrm{Re}(\lambda_{\mathbf{M}_z})) \sim 3 \cdot 10^{-2}$ for Xiao-Gimbutas and $\max(\mathrm{Re}(\lambda_{\mathbf{M}_z})) \sim 4 \cdot 10^{-3}$ for NCO. Using the NCO instead of the Shunn-Ham rule for the SP location did not influence the stability.

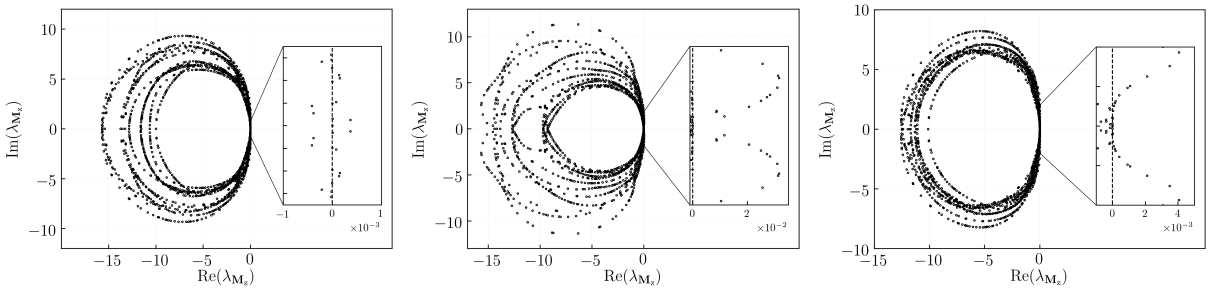

(a) Jakowiec-Sukumar rule (b) Xiao-Gimbutas rule (c) NCO rule

Figure 3: Spectrum of matrix $\mathbf{M}_z$ for unstable SDRT_2 schemes on tetrahedral elements, $(\theta_1, \theta_2) = (0, 0)$

For $p > 2$, the SDRT stability has been studied using the position of physical interior FP as Shunn-Ham, NCO and Vioreanu-Rokhlin quadrature rules while using the Williams-Shunn-Jameson quadrature rule points as the face FP. None of these rules have been able to lead to stable formulations, with a $\max(\mathrm{Re}(\lambda_{\mathbf{M}_z}))$ of $\sim 80, 400$ and 5000 for $p = 3, 4$ and 5 (respectively).

The SDRT scheme on tetrahedral elements is demonstrated as linearly stable under a Fourier analysis up to the third-order of accuracy, provided that the interior FP location is defined according to the Shunn-Ham quadrature rule.

3.4. Influence of Flux Points Located on Faces

It has been mentioned in the previous section that using different SP locations (either the NCO or the Shunn-Ham rule) did not influence the stability. Actually, it led to the exact same value of $\max\left(\mathrm{Re}(\lambda_{\mathbf{M}_z})\right)$. This result extends the statement that the SP location has no impact on the stability to tetrahedra. However, the influence of FP located on faces has not been studied yet. To do so, the SP location is fixed at the Shunn-Ham rule [12] whereas different locations of interior FP and FP located on faces are studied.

For $p = 3$, there are 10 FP located on each face (denoted Face FP). Several location are studied: the 10-points quadrature rules on a triangle from Williams-Shunn-Jameson (WSJ) [26] and Vioreanu-Rokhlin (VR) [28]) and the set of 10-points determined using the optimization process in [21], denoted OPT. For interior FP, the three quadrature rules on a tetrahedron introduced in Sec. 3.3 are considered: the Shunn-Ham [12], the Vioreanu-Rokhlin (VR) [28] and the Newton-Cotes Open (NCO) [27] quadrature rules.

Table 2 shows values of $\max(\mathrm{Re}(\lambda_{\mathbf{M}_z}))$ for all the possible combinations of FP locations. They were obtained using $(\theta_1, \theta_2, \vartheta_1, \vartheta_2) = (0, 0, 0, 0)$ and $\kappa \in [0, \pi], \Delta\kappa = \pi/32$. From this table, the impact of the position of the FP located on faces is clearly highlighted. The impact of the Face FP is even more important than the impact of interior FP: the interval of values obtained by changing the Face FP location is larger than by changing the interior FP location.

Interior FP \ Face FP	WSJ [26]	VR [28]	OPT
Shunn-Ham [12]	78.41	156.04	70.53
VR [28]	79.17	153.82	72.59
NCO [27]	68.74	110.68	95.92

Table 2: Impact of the FP located on faces: values of $\max(\mathrm{Re}(\lambda_{\mathbf{M}_z}))$ for SDRT_3, $(\theta_1, \theta_2, \vartheta_1, \vartheta_2) = (0, 0, 0, 0)$

3.5. Fourier Analysis of the Coupled Time-Space Discretization

To investigate the linear stability of the coupled time-space discretization, the semi-discretized form needs to be integrated in time. A general m-stage Runge-Kutta (RK) method for a differential equation can be written as in [36]:

$$u^{(n+1)} = u^n + \sum_{j=1}^{m} \gamma_j \, \Delta t^j \, \frac{\partial^j u^n}{\partial t^j}. \tag{34}$$

In this paper, the time-integration scheme used is the RKo6s, which is part of the low storage RK schemes optimized to ensure low dissipation and low dispersion properties given by Bogey and Bailly in [36].

The semi-discretized matrix form containing the planar harmonic wave given by Eq. (33) integrated in time using Eq. (34) is:

$$\begin{aligned} \tilde{\mathbf{U}}^{(n+1)} &= \left(\mathbf{I} + \sum_{j=1}^{m} \gamma_j \nu^j \mathbf{M}_z^j \right) \tilde{\mathbf{U}}^{(n)} \\ \Leftrightarrow \tilde{\mathbf{U}}^{(n+1)} &= \mathbf{G} \tilde{\mathbf{U}}^{(n)}. \end{aligned} \tag{35}$$

where ν is the CFL number defined by:

$$\nu = \frac{\|\mathbf{c}\| \Delta t}{\Delta x}. \tag{36}$$

The stability condition on the coupled time-space discretization is thus obtained by requiring that the amplitude of any harmonic does not grow in time, i.e.:

$$|\mathbf{G}| = \left| \frac{\tilde{\mathbf{U}}^{(n+1)}}{\tilde{\mathbf{U}}^{(n)}} \right| \leq 1. \tag{37}$$

In other words, to ensure a stable discretization, the spectral radius of the matrix $\mathbf{G}$, denoted $\rho_{\mathbf{G}}$ should be lower than 1, meaning that all the eigenvalues $\lambda_{\mathbf{G}}$ should be in the unit circle of the complex plane. The transfer matrix $\mathbf{G}$ between time steps n and $n+1$ is the amplification factor (or the Fourier symbol) of the full discretization.

The Fourier analysis of the coupled time-space discretization is conducted on tetrahedral elements for SDRT_1 and SDRT_2. The interior FP locations are in both cases taken as following the Shunn-Ham quadrature rule. Additionally to the SP and FP locations, the matrix $\mathbf{M}_z$ depends on the advection velocity defined by (θ_1, θ_2), the grid frequency κ and the harmonic wave orientation angles $(\vartheta_1, \vartheta_2)$. These parameters are taken as:

- $\theta_1 \in [0, 2\pi], \Delta\theta_1 = \pi/8,$
- $\theta_2 \in [0, 2\pi], \Delta\theta_2 = \pi/8,$
- $\kappa \in [0, \pi], \Delta\kappa = \pi/8,$
- $\vartheta_1 \in [0, 2\pi], \Delta\vartheta_1 = \pi/8,$
- $\vartheta_2 \in [0, 2\pi], \Delta\vartheta_2 = \pi/8.$

The CFL stability limits are given for those parameters in Table 3. To the authors' knowledge, there is no consensus on the definition on an equivalent CFL number for high-order discontinuous methods on simplex cells. The classical CFL definition given by Eq. (36) is thus preferred here.

(θ_1, θ_2)	$(0,0)$	$(\pi/8, \pi/8)$	$(\pi/4, \pi/4)$	$[0, 2\pi]^2$
SDRT_1	0.458	0.394	0.382	0.380
SDRT_2	0.275	0.243	0.235	0.235

Table 3: CFL stability limits ν for SDRT schemes on tetrahedra coupled with the RKo6s temporal schemes

4. Numerical Experiments

4.1. Euler Equations

We consider the three-dimensional Euler equations:

$$\frac{\partial \mathbf{u}}{\partial t} + \frac{\partial \mathbf{f}}{\partial x} + \frac{\partial \mathbf{g}}{\partial y} + \frac{\partial \mathbf{h}}{\partial z} = 0, \ \text{ in } \Omega \times [0, t_f], \tag{38}$$

where $\mathbf{u}$, $\mathbf{f}$, $\mathbf{g}$ and $\mathbf{h}$ are given by:

$$\mathbf{u} = \begin{pmatrix} \rho \\ \rho U \\ \rho V \\ \rho W \\ E \end{pmatrix}, \ \mathbf{f} = \begin{pmatrix} \rho U \\ \rho U^2 + P \\ \rho UV \\ \rho UW \\ U(E+P) \end{pmatrix}, \ \mathbf{g} = \begin{pmatrix} \rho V \\ \rho VU \\ \rho V^2 + P \\ \rho VW \\ V(E+P) \end{pmatrix}, \ \mathbf{h} = \begin{pmatrix} \rho W \\ \rho WU \\ \rho WV \\ \rho W^2 + P \\ W(E+P) \end{pmatrix}. \tag{39}$$

In Eq. (39), ρ is the density, U (respectively V, W) is the velocity component in the x (respectively y, z) direction, E is the total energy and P is the pressure determined from the following equation of state:

$$P = (\gamma - 1)\left(E - \frac{1}{2}\rho(U^2 + V^2 + W^2)\right), \tag{40}$$

where the constant ratio of specific heats γ is equal to 1.4 for air.

To validate the SDRT scheme implementation on tetrahedral elements, a 3D period Euler test case from [37, 38] is considered. The 3D Euler equations are solved on a cubic computational domain $\Omega = [0, L]^3$ where $L = 2\,\text{m}$ with periodic boundary conditions. The initial solution is:

$$\rho = 1 + 0.2\sin(\pi(x + y + z)), \quad (U, V, W, P) = (1, 1, 1, 1). \tag{41}$$

The density initial condition is displayed on Fig. 4 for a regular $10 \times 10 \times 10$ tetrahedral grid using $p = 2$.

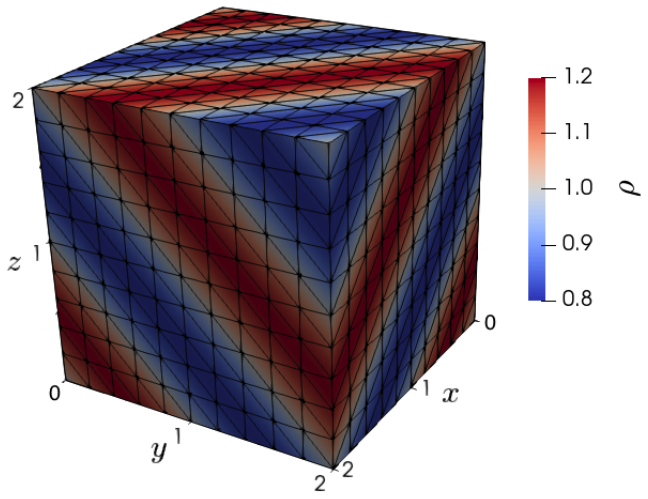

Figure 4: Initial density condition on a $10 \times 10 \times 10$ regular tetrahedral grid using $p = 2$

The solution is advanced in time using the RKo6s temporal scheme and the simulation is carried out until $t_f = 1\,\text{s}$. The time step is chosen sufficiently small so that the error from the time discretization is negligible compared to the spatial discretization error by setting the CFL number to 10^{-2}. The analytical solution of the density at any time t [38] is:

$$\rho_a = 1 + 0.2\sin(\pi(x + y + z - t(U + V + W))), \tag{42}$$

whereas velocity and pressure remain constant in time.

The convergence study was conducted on two types of grids (regular and irregular). Each mesh is refined several times and the order of accuracy is verified by computing the density L_2 error using the 84 points quadrature rule from [26]. Table 4 shows the L_2 errors and orders of accuracy for the two different types of grids (regular and irregular). For both second- and third-order schemes, a $p + 1$ order of accuracy is recovered.

p	Regular mesh			Irregular mesh		
	DoF number	L_2 error	Order of accuracy	DoF number	L_2 error	Order of accuracy
1	3000	2.183E-02	-	2132	7.713E-02	-
	24000	5.754E-03	1.92	11792	2.988E-02	1.66
	81000	2.582E-03	1.98	36460	1.437E-02	1.95
	192000	1.458E-03	1.99	82164	8.349E-03	2.00
	375000	9.345E-04	1.99	151448	5.448E-03	2.09
2	7500	1.366E-03	-	5330	2.156E-02	-
	60000	1.508E-04	3.18	29480	3.277E-03	3.30
	202500	4.343E-05	3.07	91150	9.946E-04	3.17
	480000	1.813E-05	3.04	205410	4.148E-04	3.23
	937500	9.233E-06	3.02	378620	2.173E-04	3.17

Table 4: L_2 error and order of accuracy values for regular and irregular tetrahedral grids

4.2. Taylor-Green Vortex

To validate the implementation of the SDRT method for the Navier-Stokes equations using tetrahedral grids, the Direct Numerical Simulation of the Taylor-Green Vortex (TGV) at Re = $\rho_\infty U_\infty L/\mu_{d\infty}$ = 1600 is considered. The TGV test case was proposed in the International Workshop on High-Order CFD Methods [39] to test the accuracy and performance of high-order methods. A three-dimensional periodic and transitional flow is considered and defined by:

$$U = U_\infty \sin\left(\frac{x}{L}\right)\cos\left(\frac{y}{L}\right)\cos\left(\frac{z}{L}\right), \tag{43}$$

$$V = -U_\infty \cos\left(\frac{x}{L}\right)\sin\left(\frac{y}{L}\right)\cos\left(\frac{z}{L}\right), \tag{44}$$

$$W = 0, \tag{45}$$

$$P = P_\infty + \frac{\rho_\infty U_\infty^2}{16}\left(\cos\left(\frac{2x}{L}\right) + \cos\left(\frac{2y}{L}\right)\right)\left(\cos\left(\frac{2z}{L}\right) + 2\right). \tag{46}$$

The flow is governed by the 3D compressible Navier-Stokes equations with constant physical properties and at low Mach number so that the obtained solutions are close to incompressible solutions. The test case conditions are summed up in Table 5.

Variable	Notation	Value	Unit
Reynolds number	Re	1600	-
Temperature	T_∞	300	K
Dynamic viscosity	$\mu_{d\infty}$	$1.846 \cdot 10^{-5}$	kg/m/s
Mach number	M_∞	0.1	-
Gas constant	R_{gas}	287.058	J/kg/K
Density	ρ_∞	$8.506 \cdot 10^{-4}$	kg/m^3
Pressure	P_∞	73.254	Pa
Ratio of specific heat	γ	1.4	-
Prandtl number	Pr	0.71	-
Reference length	L	1.0	m

Table 5: Flow conditions for the TGV test case

The computational domain is a cube defined by $\Omega = [-\pi L, \pi L]^3$ and periodic boundary conditions are imposed in the three directions. The SDRT implementation for interior FP is based on the Shunn-Ham quadrature rule. Diffusive flux are computed following the very same procedure given for triangular cells in [19, 21] using a centered formulation [40]. Solutions are time-integrated using the RKo6s temporal scheme and the time step Δt is imposed. Roe's Riemann solver is used to compute flux at cell interfaces. Computations are carried out on 600 processors. Three different regular grids (M_1, M_2 and M_3) are considered. Their number of elements and associated time steps are given in Table 6.

Scheme	Mesh	Number of Elements	DOF Number	Δt (sec)
	M_1	663,552	2,654,208	$7.5 \cdot 10^{-5}$
$SDRT_1$	M_2	1,572,864	6,291,456	$5.5 \cdot 10^{-5}$
	M_3	3,072,000	12,288,000	$4.5 \cdot 10^{-5}$
	M_1	663,552	6,635,520	$4.5 \cdot 10^{-5}$
$SDRT_2$	M_2	1,572,864	15,728,640	$3.5 \cdot 10^{-5}$
	M_3	3,072,000	30,720,000	$3.0 \cdot 10^{-5}$

Table 6: Computational conditions for the TGV test case

The physical duration of the computation is based on the characteristic convective time $t_c = L/U_\infty$ and is set to $t_f = 20t_c$. The kinetic energy dissipation rate ε is computed for $t \in [0, t_f]$ and compared to a reference incompressible flow solution obtained using a dealiased pseudo-spectral code (developed at Universit Catholique de Louvain, UCL) on a 512^3 mesh and provided by the International Workshop on High-Order CFD Methods [39]. The reference data is denoted 'Spectral-512^3'. To compute the kinetic energy dissipation rate, one first needs to compute the kinetic energy E_k, defined by:

$$E_k(t) = \int_\Omega \frac{1}{2}\rho(U^2 + V^2 + W^2)\mathrm{d}\Omega. \tag{47}$$

The kinetic energy is computed at each time t as:

$$E_k(t) = \sum_{i=1}^{N}\sum_{j=1}^{N_q} \omega_j |J^{(i,j)}| E_k^{(i)}(\boldsymbol{\xi}_j), \tag{48}$$

where $|J^{(i,j)}|$ is the Jacobian determinant at the j-th integration point of the i-th cell and N_q is the number of quadrature points. The quadrature points are located at $\boldsymbol{\xi}_j$ and associated with the weight ω_j. The integration is performed using the 84 points quadrature rule from [26]. The kinetic energy dissipation rate is defined by:

$$\varepsilon(t) = -\frac{\mathrm{d}E_k}{\mathrm{d}t}(t), \tag{49}$$

and is computed using a first-order upwind scheme. The kinetic energy dissipation rate is rendered dimensionless by $\varepsilon_c = E_k(t=0)/t_c$. Results obtained with the second and third-order SDRT schemes are compared with reference data in Fig. 5. Using the second-order SDRT scheme (Fig. 5a), the dimensionless kinetic energy dissipation rate $\varepsilon/\varepsilon_c$ evolution is first quite accurate ($t/t_c \in [0,3]$) but grows too fast from $t/t_c > 3$ for all grid resolutions. The maximal peak value is underestimated (of 4% for M_1 and 7% for M_2 and M_3) and shifted (of 8% for M_1 and M_2 and 5% for M_3). However, results get closer to the reference data as the number of DOF increases. Using the second-order SDRT scheme leads to better results (Fig. 5b). For $t/t_c \in [0,9]$, results obtained using the M_1 mesh slightly overestimate $\varepsilon/\varepsilon_c$ whereas results on M_2 and M_3 grids show an excellent agreement with the reference data. The improvement of the solution accuracy when the number of DOF increases can be clearly seen at $t/t_c = 9$. Compared to the reference data, the peak value is particularly well predicted on the M_3 mesh (underestimation of 0.7%). For $t/t_c \in [12,17]$, $\varepsilon/\varepsilon_c$ is a little overestimated but the final value at $t/t_c = 20$ matches the reference.

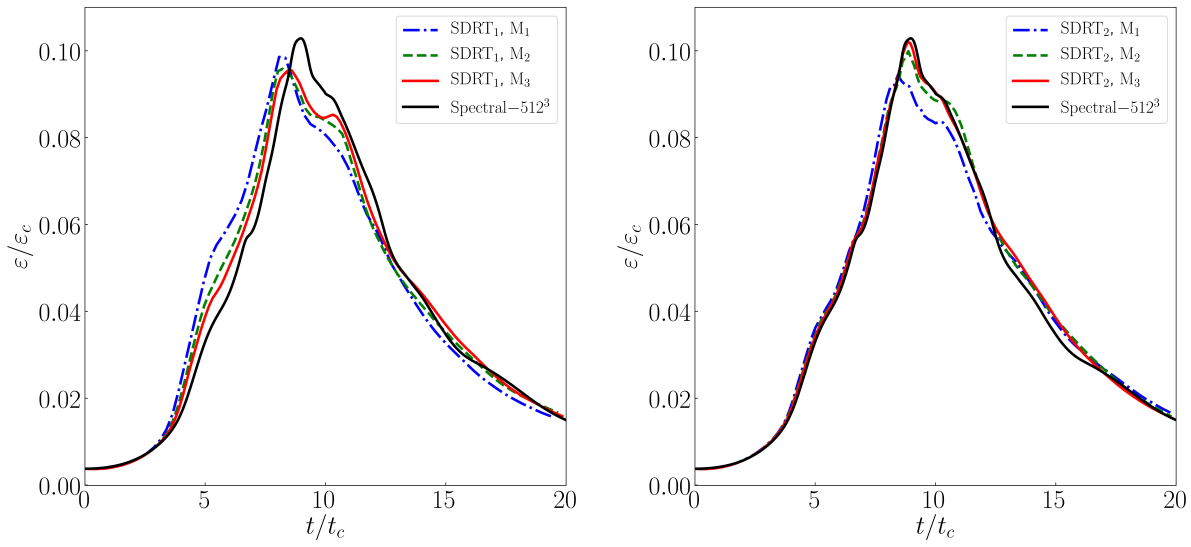

(a) $SDRT_1$ (b) $SDRT_2$

Figure 5: Dimensionless kinetic energy dissipation rate obtained with second and third-order SDRT schemes compared to reference data

5. Conclusion

Tetrahedrons are the reference elements for automatic mesh generation on complex geometries and they are widely used in the case of mesh adaptation. Accounting for tetrahedral cells is today essential for a numerical scheme to be usable on unstructured grids.

When using the weak formulation associated with the Discontinuous Galerkin formulation, stability is ensured. When one studies formulations based on the strong form of the equations, stability was demonstrated for tetrahedral cells considering the Flux Reconstruction (FR) or the Correction Procedure for Reconstruction (CPR). In this context, the present paper introduces a new formulation usable on tetrahedrons, following the Spectral Difference method. The idea is to define the flux vector in the Raviart-Thomas space, rather than the flux components in the Lagrange space. Such a procedure changes essentially the definition of the flux polynomial approximation: the procedure is vector-based and not component-based. A simple analysis of the number of interior flux points shows that the proposed scheme and the Flux Reconstruction method will always differ.

The key point remains the position of the flux points since this position significantly influences the scheme stability. It was demonstrated in the paper that using Shunn-Ham quadrature rule points as interior flux

points and Williams-Shunn-Jameson quadrature rule points as face flux points leads to a stable formulation for polynomial degrees of $p = 1$ and $p = 2$, leading to an order of accuracy of 2 and 3.

For $p > 2$, several quadrature rule sets of points were tested as interior flux points while keeping the Williams-Shunn-Jameson points as face flux points but none of them lead to a stable formulation. Such a result does not mean that a stable formulation does not exist but states the fact that additional research is required. In particular, the influence of the flux points located on faces was highlighted in this paper and their location should be taken into account to determine stable formulations. Changing their location will not imply the use of mortar techniques between a tetrahedral and a prismatic element as long as the solution points location of a triangle is chosen to be the same as the flux points on a tetrahedral face. Since the solution points do not influence the stability, this requirement can easily be fulfilled.

Finally, the procedure was validated for Euler and Navier-Stokes equations on academic cases. Future efforts concern an extensive validation on more complex configurations up to the third-order of accuracy and research of stable formulations for $p > 2$.

Appendix A. Definition of the Raviart-Thomas (RT) space

The Raviart-Thomas (RT) finite element spaces were originally introduced by Raviart and Thomas [41] to approximate the Sobolev space H(div) defined by:

$$\mathrm{H(div)} = \{u \in \left(L^2(K)\right)^d,\ \nabla \cdot u \in L^2(K)\}, \tag{A.1}$$

where d is the dimension, K is a bounded open subset of $\mathbb{R}^d$ with a Lipshitz continuous boundary, $L^2(K)$ is the Hilbert space of square-integrable function defined on K. The extension to the three-dimensional case considering K as a tetrahedron or a cube was proposed by Nedelec [42]. The space RT_p spanned by the Raviart-Thomas basis functions of degree p is the smallest polynomial space such that the divergence maps RT_p onto $\mathbb{P}_p$, the space of piecewise polynomials of degree $\leq p$. Considering the reference tetrahedron $\mathcal{T}_e$, the RT space of order p is defined in 3D by:

$$RT_p = (\mathbb{P}_p)^3 + \begin{pmatrix} x \\ y \\ z \end{pmatrix} \bar{\mathbb{P}}_p, \tag{A.2}$$

where $\mathbb{P}_p$ is the space of polynomials of degree at most p:

$$\mathbb{P}_p(x, y, z) = span\{x^i y^j z^k,\ i, j, k \geq 0, i + j + k \leq p\}, \tag{A.3}$$

$\bar{\mathbb{P}}_p$ is the space of polynomials of degree p:

$$\bar{\mathbb{P}}_p(x, y, z) = span\{x^i y^j z^k,\ i, j, k \geq 0, i + j + k = p\}, \tag{A.4}$$

and $(\mathbb{P}_p)^3 = (\mathbb{P}_p, \mathbb{P}_p, \mathbb{P}_p)^\intercal$ is the three dimensional vector space for which each component is a polynomial of degree at most p. The dimension of each space is dim $\mathbb{P}_p = \frac{(p+1)(p+2)(p+3)}{6}$, dim $\mathbb{P}_p^3 = \frac{(p+1)(p+2)(p+3)}{2}$, dim $\bar{\mathbb{P}}_p = \frac{(p+1)(p+2)}{2}$ and thus dim $RT_p = \frac{(p+1)(p+2)(p+4)}{2}$. We denote $\boldsymbol{\phi}_n, n \in [\![1, N_{FP}]\!]$ the monomials which form a basis in the RT_p space where

$$N_{FP} = \frac{(p + 1)(p + 2)(p + 4)}{2}. \tag{A.5}$$

Determination of $\boldsymbol{\phi}_n$ for RT_1, $N_{FP} = 15$

$$\boldsymbol{\phi} = \{\phi_1, \cdots, \phi_{15}\} = \left\{ \begin{pmatrix} 1 \\ 0 \\ 0 \end{pmatrix}, \begin{pmatrix} x \\ 0 \\ 0 \end{pmatrix}, \begin{pmatrix} y \\ 0 \\ 0 \end{pmatrix}, \begin{pmatrix} z \\ 0 \\ 0 \end{pmatrix}, \begin{pmatrix} 0 \\ 1 \\ 0 \end{pmatrix}, \begin{pmatrix} 0 \\ x \\ 0 \end{pmatrix}, \begin{pmatrix} 0 \\ y \\ 0 \end{pmatrix}, \begin{pmatrix} 0 \\ z \\ 0 \end{pmatrix}, \begin{pmatrix} 0 \\ 0 \\ 1 \end{pmatrix}, \begin{pmatrix} 0 \\ 0 \\ x \end{pmatrix}, \begin{pmatrix} 0 \\ 0 \\ y \end{pmatrix}, \begin{pmatrix} 0 \\ 0 \\ z \end{pmatrix}, \begin{pmatrix} x^2 \\ xy \\ xz \end{pmatrix}, \begin{pmatrix} yx \\ y^2 \\ yz \end{pmatrix}, \begin{pmatrix} zx \\ zy \\ z^2 \end{pmatrix} \right\}. \tag{A.6}$$

Appendix B. Matrices Formulation for the Fourier Analysis

The matrices $\mathbf{M}^{0,0,0}$, $\mathbf{M}^{-1,0,0}$, $\mathbf{M}^{+1,0,0}$, $\mathbf{M}^{0,-1,0}$, $\mathbf{M}^{0,+1,0}$, $\mathbf{M}^{0,0,-1}$ and $\mathbf{M}^{0,0,+1}$ involved in the SDRT spatial discretization for the Fourier analysis on tetrahedral elements (Eq. (28)) are detailed in this appendix. Those matrices are given as:

$$\mathbf{M}^{0,0,0} = \begin{bmatrix} \mathbf{D}_{jk} & \cdots & O_{N_{SP},N_{FP}} \\ \vdots & \ddots & \vdots \\ O_{N_{SP},N_{FP}} & \cdots & \mathbf{D}_{jk} \end{bmatrix} \mathbf{C}^{0,0,0} \begin{bmatrix} \mathbf{T}_{kj} & \cdots & O_{N_{FP},N_{SP}} \\ \vdots & \ddots & \vdots \\ O_{N_{FP},N_{SP}} & \cdots & \mathbf{T}_{kj} \end{bmatrix}, \tag{B.1}$$

where $O_{m,n}$ is the zero matrix of size $m \times n$. The same goes for $\mathbf{M}^{-1,0,0}$, $\mathbf{M}^{+1,0,0}$, $\mathbf{M}^{0,-1,0}$, $\mathbf{M}^{0,+1,0}$, $\mathbf{M}^{0,0,-1}$ and $\mathbf{M}^{0,0,+1}$, associated respectively to the velocity matrices $\mathbf{C}^{-1,0,0}$, $\mathbf{C}^{+1,0,0}$, $\mathbf{C}^{0,-1,0}$, $\mathbf{C}^{0,+1,0}$, $\mathbf{C}^{0,0,-1}$ and $\mathbf{C}^{0,0,+1}$. The transfer matrix is given by Eq. (16):

$$\mathbf{T}_{kj} = \sum_{m=1}^{N_{SP}^{tet}} \left(\Phi_m(\boldsymbol{\xi}_j)\right)^{-1} \Phi_m(\boldsymbol{\xi}_k), \tag{B.2}$$

and the differentiation matrix by Eq. (21):

$$\mathbf{D}_{jk} = \sum_{n=1}^{N_{FP}^{tet}} \left(\boldsymbol{\phi}_n(\boldsymbol{\xi}_k) \cdot \hat{\mathbf{n}}_k\right)^{-1} \hat{\nabla} \cdot \boldsymbol{\phi}_n(\boldsymbol{\xi}_j). \tag{B.3}$$

The velocity matrices are given as:

$$\mathbf{C}^{0,0,0} = \begin{bmatrix} \mathbf{C}^{L} & \mathbf{C}^{T_1,T_2} & O_{N_{FP},N_{FP}} & O_{N_{FP},N_{FP}} & O_{N_{FP},N_{FP}} & \mathbf{C}^{T_1,T_6} \\ \mathbf{C}^{T_2,T_1} & \mathbf{C}^{L} & \mathbf{C}^{T_2,T_3} & O_{N_{FP},N_{FP}} & O_{N_{FP},N_{FP}} & O_{N_{FP},N_{FP}} \\ O_{N_{FP},N_{FP}} & \mathbf{C}^{T_3,T_2} & \mathbf{C}^{L} & \mathbf{C}^{T_3,T_4} & O_{N_{FP},N_{FP}} & O_{N_{FP},N_{FP}} \\ O_{N_{FP},N_{FP}} & O_{N_{FP},N_{FP}} & \mathbf{C}^{T_4,T_3} & \mathbf{C}^{L} & \mathbf{C}^{T_4,T_5} & O_{N_{FP},N_{FP}} \\ O_{N_{FP},N_{FP}} & O_{N_{FP},N_{FP}} & O_{N_{FP},N_{FP}} & \mathbf{C}^{T_5,T_4} & \mathbf{C}^{L} & \mathbf{C}^{T_5,T_6} \\ \mathbf{C}^{T_6,T_1} & O_{N_{FP},N_{FP}} & O_{N_{FP},N_{FP}} & O_{N_{FP},N_{FP}} & \mathbf{C}^{T_6,T_5} & \mathbf{C}^{L} \end{bmatrix}, \tag{B.4}$$

$$\mathbf{C}^{-1,0,0} = \begin{bmatrix} O_{N_{FP},N_{FP}} & O_{N_{FP},N_{FP}} & O_{N_{FP},N_{FP}} & O_{N_{FP},N_{FP}} & \mathbf{C}^{T_1,T_5} & O_{N_{FP},N_{FP}} \\ O_{N_{FP},N_{FP}} & O_{N_{FP},N_{FP}} & O_{N_{FP},N_{FP}} & \mathbf{C}^{T_2,T_4} & O_{N_{FP},N_{FP}} & O_{N_{FP},N_{FP}} \\ & & \begin{bmatrix} O_{4N_{FP},6N_{FP}} \end{bmatrix} & & & \end{bmatrix}, \tag{B.5}$$

$$\mathbf{C}^{+1,0,0} = \begin{bmatrix} & & \begin{bmatrix} O_{3N_{FP},6N_{FP}} \end{bmatrix} & & & \\ O_{N_{FP},N_{FP}} & \mathbf{C}^{T_4,T_2} & O_{N_{FP},N_{FP}} & O_{N_{FP},N_{FP}} & O_{N_{FP},N_{FP}} & O_{N_{FP},N_{FP}} \\ \mathbf{C}^{T_5,T_1} & O_{N_{FP},N_{FP}} & O_{N_{FP},N_{FP}} & O_{N_{FP},N_{FP}} & O_{N_{FP},N_{FP}} & O_{N_{FP},N_{FP}} \\ & & \begin{bmatrix} O_{N_{FP},6N_{FP}} \end{bmatrix} & & & \end{bmatrix}, \tag{B.6}$$

$$\mathbf{C}^{0,-1,0} = \begin{bmatrix} & & \begin{bmatrix} O_{2N_{FP},6N_{FP}} \end{bmatrix} & & & \\ \mathbf{C}^{T_3,T_1} & O_{N_{FP},N_{FP}} & O_{N_{FP},N_{FP}} & O_{N_{FP},N_{FP}} & O_{N_{FP},N_{FP}} & O_{N_{FP},N_{FP}} \\ O_{N_{FP},N_{FP}} & O_{N_{FP},N_{FP}} & O_{N_{FP},N_{FP}} & O_{N_{FP},N_{FP}} & O_{N_{FP},N_{FP}} & \mathbf{C}^{T_4,T_6} \\ & & \begin{bmatrix} O_{2N_{FP},6N_{FP}} \end{bmatrix} & & & \end{bmatrix}, \tag{B.7}$$

$$\mathbf{C}^{0,+1,0} = \begin{bmatrix} O_{N_{FP},N_{FP}} & O_{N_{FP},N_{FP}} & \mathbf{C}^{T_1,T_3} & O_{N_{FP},N_{FP}} & O_{N_{FP},N_{FP}} & O_{N_{FP},N_{FP}} \\ & & \begin{bmatrix} O_{4N_{FP},6N_{FP}} \end{bmatrix} & & & \\ O_{N_{FP},N_{FP}} & O_{N_{FP},N_{FP}} & O_{N_{FP},N_{FP}} & \mathbf{C}^{T_6,T_4} & O_{N_{FP},N_{FP}} & O_{N_{FP},N_{FP}} \end{bmatrix}, \tag{B.8}$$

$$\mathbf{C}^{0,0,-1} = \begin{bmatrix} & & \begin{bmatrix} O_{N_{FP},6N_{FP}} \end{bmatrix} & & & \\ O_{N_{FP},N_{FP}} & O_{N_{FP},N_{FP}} & O_{N_{FP},N_{FP}} & O_{N_{FP},N_{FP}} & O_{N_{FP},N_{FP}} & \mathbf{C}^{T_2,T_6} \\ O_{N_{FP},N_{FP}} & O_{N_{FP},N_{FP}} & O_{N_{FP},N_{FP}} & O_{N_{FP},N_{FP}} & \mathbf{C}^{T_3,T_5} & O_{N_{FP},N_{FP}} \\ & & \begin{bmatrix} O_{3N_{FP},6N_{FP}} \end{bmatrix} & & & \end{bmatrix}, \tag{B.9}$$

$$\mathbf{C}^{0,0,+1} = \begin{bmatrix} & & \begin{bmatrix} O_{4N_{FP},6N_{FP}} \end{bmatrix} & & & \\ O_{N_{FP},N_{FP}} & O_{N_{FP},N_{FP}} & \mathbf{C}^{T_5,T_3} & O_{N_{FP},N_{FP}} & O_{N_{FP},N_{FP}} & O_{N_{FP},N_{FP}} \\ O_{N_{FP},N_{FP}} & \mathbf{C}^{T_6,T_2} & O_{N_{FP},N_{FP}} & O_{N_{FP},N_{FP}} & O_{N_{FP},N_{FP}} & O_{N_{FP},N_{FP}} \end{bmatrix}, \tag{B.10}$$

where $\mathbf{C}^L$ is defined by:

$$\mathbf{C}^L = \begin{bmatrix} \begin{bmatrix} (\mathbf{c}\cdot\mathbf{n})\frac{1+\text{sign}(\mathbf{c}\cdot\mathbf{n})}{2} & \cdots & 0 \\ \vdots & \ddots & \vdots \\ 0 & \cdots & (\mathbf{c}\cdot\mathbf{n})\frac{1+\text{sign}(\mathbf{c}\cdot\mathbf{n})}{2} \end{bmatrix}_{4N_f,4N_f} & O_{4N_f,N_i} \\ O_{N_i,4N_f} & \begin{bmatrix} |J|J^{-1}(\mathbf{c}\cdot\hat{\mathbf{n}}) & \cdots & 0 \\ \vdots & \ddots & \vdots \\ 0 & \cdots & |J|J^{-1}(\mathbf{c}\cdot\hat{\mathbf{n}}) \end{bmatrix}_{N_i,N_i} \end{bmatrix}. \tag{B.11}$$

The matrix $\mathbf{C}^{T_i,T_j}$ links the FP between the triangular faces of T_i and T_j. Its expression will depend on the local connectivity, i.e. the number and the orientation of the two faces in their respective element. The face number gives the local FP numbering whereas the orientation (how the two faces are facing each other) gives the FP order. An example of its determination is provided below for two arbitrary tetrahedral elements.

Determination of the Matrix $\mathbf{C}^{\mathbf{T_i},\mathbf{T_j}}$ - Example for $\mathbf{p = 1}$ Let us consider two tetrahedron T_1 and T_2 defined by their four nodes:

$$T_1: \quad N_1, N_2, N_3, N_4 = A, B, C, D, \tag{B.12}$$

$$T_2: \quad N_1, N_2, N_3, N_4 = A, C, E, D. \tag{B.13}$$

Following the CGNS notations, their faces are defined by:

- T_1, Face 1: A, C, B,
- T_1, Face 2: A, B, D,
- T_1, Face 3: B, C, D,
- T_1, Face 4: C, A, D,
- T_2, Face 1: A, E, C,
- T_2, Face 2: A, C, D,
- T_2, Face 3: C, E, D,
- T_2, Face 4: E, A, D.

They are sharing a face corresponding to Face 4 in T_1 and Face 2 in T_2. In the case of $p = 1$, this indicates that the FP numbers on (T_1, Face 4) are $[10, 12]$ whereas the FP number (Face 2, T_2) are $[4, 6]$. Then, the orientation between the faces needs to be determined to know in which order the FP are facing each other. For two arbitrary faces A and B defined respectively by nodes (A_1, A_2, A_3) and (B_1, B_2, B_3), three cases are possible:

- $A_1 = B_3$, $A_2 = B_2$, $A_3 = B_1$,
- $A_1 = B_2$, $A_2 = B_1$, $A_3 = B_3$,
- $A_1 = B_1$, $A_2 = B_3$, $A_3 = B_2$.

Our example is illustrated in Fig. 6 and corresponds to the second case.

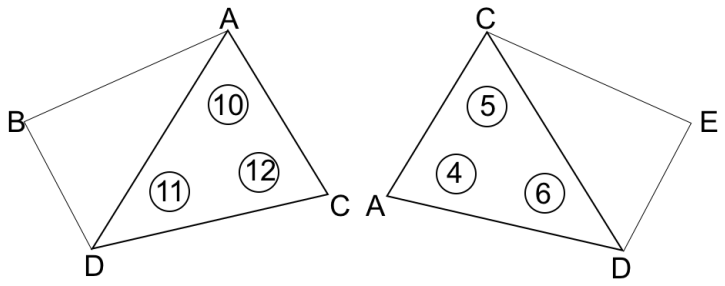

Figure 6: Illustration of the orientation determination: T_1 (on the left) and T_2 (on the right)

In this example, the matrix $\mathbf{C}^{T_1,T_2}$ will take the following expression:

$$\mathbf{C}^{T_1,T_2} = (\mathbf{c}\cdot\mathbf{n})\begin{bmatrix}\begin{bmatrix} O_{N_f,N_f} & \begin{bmatrix} 0 & \frac{1+\text{sign}(\mathbf{c}\cdot\mathbf{n})}{2} & 0 \\ 0 & 0 & \frac{1+\text{sign}(\mathbf{c}\cdot\mathbf{n})}{2} \\ \frac{1+\text{sign}(\mathbf{c}\cdot\mathbf{n})}{2} & 0 & 0 \end{bmatrix} & O_{N_f,2*N_f+N_i} \end{bmatrix} \\ \begin{matrix} O_{3N_f,N_{FP}} \\ O_{N_i,N_{FP}} \end{matrix} \end{bmatrix}. \tag{B.14}$$

Declarations

Funding. The authors did not receive support from any organization for the submitted work.

Conflicts of interests. The authors have no conflicts of interest to declare that are relevant to the content of this article.

Availability of data and material. The datasets generated during and/or analyzed during the current study are available from the corresponding author on reasonable request.

References

[1] J. S. Hesthaven, C. H. Teng, Stable Spectral Methods on Tetrahedral Elements, SIAM Journal on Scientific Computing 21 (6) (2000) 2352–2380. doi:10.1137/S1064827598343723.

[2] J. Hesthaven, T. Warburton, Nodal High-Order Methods on Unstructured Grids: I. Time-Domain Solution of Maxwell's Equations, Journal of Computational Physics 181 (1) (2002) 186–221. doi:10.1006/jcph.2002.7118.

[3] P. Bettess, O. Laghrouche, E. Perrey-Debain, J. S. Hesthaven, T. Warburton, High-order nodal discontinuous Galerkin methods for the Maxwell eigenvalue problem, Philosophical Transactions of the Royal Society of London. Series A: Mathematical, Physical and Engineering Sciences 362 (1816) (2004) 493–524. doi:10.1098/rsta.2003.1332.

[4] J. S. Hesthaven, T. Warburton, Nodal Discontinuous Galerkin Methods, Springer New York, 2008. doi:10.1007/978-0-387-72067-8.

[5] S. Dosopoulos, B. Zhao, J.-F. Lee, Non-Conformal and Parallel Discontinuous Galerkin Time Domain Method for Maxwell's Equations: EM Analysis of IC Packages, Journal of Computational Physics 238 (2013) 48–70. doi:10.1016/j.jcp.2012.11.048.

[6] J. Chan, Z. Wang, A. Modave, J. Remacle, T. Warburton, GPU-accelerated discontinuous Galerkin methods on hybrid meshes, Journal of Computational Physics 318 (2016) 142–168. doi:10.1016/j.jcp.2016.04.003.

[7] H. T. Huynh, A Flux Reconstruction Approach to High-Order Schemes Including Discontinuous Galerkin Methods, in: 18th AIAA Computational Fluid Dynamics Conference, 2007. doi:10.2514/6.2007-4079.

[8] P. E. Vincent, P. Castonguay, A. Jameson, A New Class of High-Order Energy Stable Flux Reconstruction Schemes, Journal of Scientific Computing 47 (1) (2011) 50–72. doi:10.1007/s10915-010-9420-z.

[9] D. M. Williams, A. Jameson, Energy Stable Flux Reconstruction Schemes for Advection-Diffusion Problems on Tetrahedra, Journal of Scientific Computing 59 (3) (2014) 721–759. doi:10.1007/s10915-013-9780-2.

[10] D. Williams, A. Jameson, Nodal Points and the Nonlinear Stability of High-Order Methods for Unsteady Flow Problems on Tetrahedral Meshes, 2013. doi:10.2514/6.2013-2830.

[11] F. D. Witherden, J. S. Park, P. E. Vincent, An Analysis of Solution Point Coordinates for Flux Reconstruction Schemes on Tetrahedral Elements, Journal of Scientific Computing 69 (2016) 905–920. doi:10.1007/s10915-016-0204-y.
[12] L. Shunn, F. Ham, Symmetric quadrature rules for tetrahedra based on a cubic close-packed lattice arrangement, Journal of Computational and Applied Mathematics 236 (17) (2012) 4348–4364. doi:10.1016/j.cam.2012.03.032.
[13] J. R. Bull, A. Jameson, Simulation of the TaylorGreen Vortex Using High-Order Flux Reconstruction Schemes, AIAA Journal 53 (9) (2015) 2750–2761. doi:10.2514/1.J053766.
[14] D. A. Kopriva, A Conservative Staggered-Grid Chebyshev Multidomain Method for Compressible Flows. II. A Semi-Structured Method, Journal of Computational Physics 128 (2) (1996) 475–488. doi:10.1006/jcph.1996.0225.
[15] Y. Liu, M. Vinokur, Z.J. Wang, Spectral Difference Method for Unstructured Grids I: Basic Formulation, Journal of Computational Physics 216 (2) (2006) 780–801. doi:10.1016/j.jcp.2006.01.024.
[16] K. Van den Abeele, C. Lacor, Z.J. Wang, On the Stability and Accuracy of the Spectral Difference Method, Journal of Scientific Computing 37 (2) (2008) 162–188. doi:10.1007/s10915-008-9201-0.
[17] A. Balan, G. May, J. Schberl, A stable high-order Spectral Difference method for hyperbolic conservation laws on triangular elements, Journal of Computational Physics 231 (5) (2012) 2359–2375. doi:10.1016/j.jcp.2011.11.041.
[18] G. May, J. Schöberl, Analysis of a Spectral Difference Scheme with Flux Interpolation on Raviart-Thomas Elements, Tech. rep., Aachen Institute for Advanced Study in Computational Engineering Science (2010).
[19] M. Li, Z. Qiu, C. Liang, M. Sprague, M. Xu, C. A. Garris, A new high-order spectral difference method for simulating viscous flows on unstructured grids with mixed-element meshes, Computers & Fluids 184 (2019) 187–198. doi:10.1016/j.compfluid.2019.03.010.
[20] Z. Qiu, B. Zhang, C. Liang, M. Xu, A high-order solver for simulating vortex-induced vibrations using sliding-mesh spectral difference method and hybrid grids, International Journal for Numerical Methods in Fluids 90 (2019) 171–194. doi:10.1002/fld.4717.
[21] A. Veilleux, G. Puigt, H. Deniau, G. Daviller, A stable Spectral Difference approach for computations with triangular and hybrid grids up to the 6^{th} order of accuracy, Journal of Computational Physics 449 (2022) 110774. doi:10.1016/j.jcp.2021.110774.
[22] A. Balan, G. May, J. Schberl, A Stable and Spectral Difference and Method for Triangles, in: 49th AIAA Aerospace Sciences Meeting including the New Horizons Forum and Aerospace Exposition, 2011. doi:10.2514/6.2011-47.
[23] J. Proriol, Sur une famille de polynômes à deux variables orthogonaux dans un triangle, Sci. Paris 257 (1957) 24592461.
[24] T. Koornwinder, Two-variable analogues of the classical orthogonal polynomials, in: R. Askey (Ed.), Theory and Applications of Special Functions, San Diego, 1975.
[25] M. Dubiner, Spectral methods on triangles and other domains, Journal of Scientific Computing 6 (4) (1991) 345–390. doi:10.1007/BF01060030.
[26] D. Williams, L. Shunn, A. Jameson, Symmetric quadrature rules for simplexes based on sphere close packed lattice arrangements, Journal of Computational and Applied Mathematics 266 (2014) 18–38. doi:10.1016/j.cam.2014.01.007.
[27] P. Silvester, Symmetric quadrature formulae for simplexes, Mathematics of Computation 24 (1970) 95–100. doi:10.1090/S0025-5718-1970-0258283-6.
[28] B. Vioreanu, V. Rokhlin, Spectra of Multiplication Operators as a Numerical Tool, SIAM Journal on Scientific Computing 36 (2014) 267–288. doi:10.1137/110860082.
[29] P. Keast, Moderate degree tetrahedral quadrature formulas, Computer Methods in Applied Mechanics and Engineering 55 (3) (1986) 339–348. doi:10.1016/0045-7825(86)90059-9.
[30] F. Witherden, P. Vincent, On the identification of symmetric quadrature rules for finite element methods, Computers and Mathematics with Applications 69 (2015) 1232–1241. doi:10.1016/j.camwa.2015.03.017.
[31] Y. Jinyun, Symmetyric Gaussian quadrature formulae for tetrahedronal regions, Computer Methods in Applied Mechanics and Engineering 43 (1984) 349–353. doi:10.1016/0045-7825(84)90072-0.
[32] P. Hammer, O. Marlowe, A. Stroud, Numerical Integration Over Simplexes and Cones, Mathematical Tables and Other Aids to Computation 10 (55) (1956) 130–137. doi:10.1090/S0025-5718-1956-0086389-6.
[33] Y. Liu, M. Vinokur, Exact integrations of polynomials and symmetric quadrature formulas over arbitrary polyhedral grids, Journal of Computational Physics 140 (1998) 122–147. doi:10.1006/jcph.1998.5884.
[34] J. Jakowiec, N. Sukumar, High-order cubature rules for tetrahedra, Numerical Methods in Engineering 121 (11) (2020) 2418–2436. doi:10.1002/nme.6313.
[35] H. Xiao, Z. Gimbutas, A numerical algorithm for the construction of efficient quadrature rules in two and higher dimensions, Computers and Mathematics with Applications 59 (2) (2010) 663–676. doi:10.1016/j.camwa.2009.10.027.
[36] C. Bogey, C. Bailly, A family of low dispersive and low dissipative explicit schemes for flow and noise computations, Journal of Computational Physics 194 (2004) 194–214. doi:10.1016/j.jcp.2003.09.003.
[37] G.-S. Jiang, C.-W. Shu, Efficient Implementation of Weighted ENO Schemes, Journal of Computational Physics 126 (1) (1996) 202–228. doi:10.1006/jcph.1996.0130.
[38] W. Pazner, P.-O. Persson, Approximate tensor-product preconditioners for very high order discontinuous Galerkin methods, Journal of Computational Physics (354) (2018) 344–369. doi:10.1016/j.jcp.2017.10.030.
[39] https://how5.cenaero.be/. [link].
URL https://how5.cenaero.be/
[40] Y. Sun, Z.J. Wang, Y. Liu, High-order multidomain spectral difference method for the Navier-Stokes equations on unstructured hexahedral grids, Communications in Computational Physics 2 (2) (2007) 310–333.
[41] P. Raviart, J. Thomas, A mixed finite element method for 2nd order elliptic problem, in: Lecture Notes in Mathematics 606, 1977, p. 292315.
[42] J. Nedelec, Mixed finite elements in R3, Numerische Mathematik 35 (1980) 315–341.